Nanoscale Horizons

ROYAL SOCIETY OF CHEMISTRY

COMMUNICATION

View Article Online
View Journal | View Issue

Check for updates

Cite this: *Nanoscale Horiz.*, 2026, **11**, 1102

Received 20th October 2025,
Accepted 6th January 2026

DOI: 10.1039/d5nh00704f

rsc.li/nanoscale-horizons

Designing bithiazole-based conjugated polymers as alternatives to benzothiadiazoles for photocatalytic hydrogen evolution

Taekmin Kim,†[a] WonJo Jeong,†[b] Sanghyeok An,[a] Junho Kim,[d] Gayoung Ham,[c] Seungok Pyo,[b] Hyojung Cha,*[c] In Hwan Jung*[b] and Dae Sung Chung*[a]

Photocatalytic hydrogen evolution on bithiazole (Tz)-based conjugated polymers was demonstrated for the first time, establishing Tz as a new building block beyond conventional benzothiadiazole (BT) systems. Two Tz-based donor–acceptor polymers were synthesized: one consisting of fluorene and Tz units (PFOTz), and the other incorporating a thiophene π-spacer between Tz units (PFOTzT). The use of thiophene-incorporating PFOTzT leads to a more ordered nanostructure within the resulting nanoparticles, promoting stronger interchain interactions and red-shifted absorption. Photocatalytic nanoparticles were prepared *via* mini-emulsion and nanoprecipitation methods with various surfactants. The hydrogen evolution reaction (HER) performance was evaluated under visible-light irradiation using ascorbic acid as the sacrificial electron donor. Both Tz-based polymers showed HER activity, but PFOTzT exhibited significantly higher HER activity. Time-resolved photoluminescence and transient absorption spectroscopy revealed that its superior performance arises from efficient exciton dissociation and suppressed charge recombination, resulting in prolonged carrier lifetimes. These results establish Tz as an alternative to BT in the design of high-performance organic photocatalysts and underscore the crucial impact of nanoscale morphology and interfacial engineering on photocatalytic efficiency.

New concepts

The development of metal-free organic photocatalysts has long relied exclusively on benzothiadiazole (BT)-based polymers, limiting structural diversity and slowing the progress of material synthesis. This work introduces bithiazole (Tz) derivatives as new electron-deficient building blocks that enable efficient water splitting using conjugated polymer photocatalysts. The incorporation of a thiophene π-spacer between Tz units demonstrates that fine-tuning nanoscale morphology can directly promote exciton dissociation and charge separation, leading to efficient hydrogen evolution under visible light. This new polymeric architecture redefines molecular design strategies for donor–acceptor conjugated polymers and broadens the molecular design space for organic photocatalysts beyond BT-centered architectures.

Introduction

Photocatalytic water splitting presents a sustainable strategy for hydrogen production using water as the feedstock, with oxygen as the only byproduct.[1–5] Inorganic semiconductors such as TiO_2, WO_3, and $SrTiO_3$ have been widely investigated for facilitating both hydrogen and oxygen evolution through reductive and oxidative half-reactions, thereby enabling overall water splitting.[6–12] However, for practical and scalable applications, photocatalysts should ideally be composed of earth-abundant and non-toxic elements. In this context, organic photocatalysts have emerged as attractive alternatives due to their tunable electronic properties, structural versatility, and solution processability.[13–19]

For efficient water splitting, the band edges of the photocatalyst must straddle the redox potentials of H^+/H_2 and H_2O/O_2, while also ensuring fast charge separation and slow recombination. In practice, co-catalysts and sacrificial electron donors are often introduced to accelerate the interfacial redox kinetics and to selectively promote the hydrogen evolution half-reaction. Therefore, the development of photocatalysts that optimize light absorption, band alignment, and charge-transport pathways is required to enhance the utilization of photogenerated carriers for efficient hydrogen production.[20,21]

Among the available organic materials, donor–acceptor (D–A) conjugated polymers have demonstrated considerable

[a] *Department of Chemical Engineering, Pohang University of Science and Technology (POSTECH), Pohang 37673, Republic of Korea. E-mail: dchung@postech.ac.kr*
[b] *Department of Organic and Nano Engineering, and Human-Tech Convergence Program, Hanyang University, Seoul 04763, Republic of Korea. E-mail: inhjung@hanyang.ac.kr*
[c] *School of Energy Engineering, Kyungpook National University, Daegu 41566, Republic of Korea. E-mail: hcha@knu.ac.kr*
[d] *Department of Energy Engineering, Hanyang University, Seoul 04763, Republic of Korea*
† These authors contributed equally to this work.

promise for photocatalytic hydrogen evolution.[22–27] In particular, benzothiadiazole (BT)-based D–A polymers—such as poly(9,9-dioctylfluorene-*alt*-1,2,3-benzothiadiazole) (F8BT)—have exhibited significant photocatalytic activity in aqueous dispersions.[28,29] The high efficiency of BT-based systems is attributed to the favorable electronic interactions between BT moieties and protons, enabling efficient proton reduction.[30,31] Numerous BT derivatives have since been investigated in combination with various electron-donating co-monomers and nanoparticle fabrication methods.[32–36] For example, a BT–thiophene copolymer exhibited strong absorption extending to 700 nm and achieved an exceptional hydrogen evolution rate (HER) of 50 ± 0.5 mmol g^{-1} h^{-1}, along with an apparent quantum yield (AQY) of 0.6% at 550 nm.[28]

Despite these advances, the development of alternative acceptor structures beyond BT for use in conjugated polymer photocatalysts remains limited.[37] Given the structural and electronic similarity of BT and bithiazole (Tz)[38] moieties, particularly their nitrogen-containing aromaticity and electron-deficient characteristics, Tz represents a promising alternative acceptor unit. Tz-based motifs have demonstrated excellent performance for other organic electronic applications;[39,40] however, to date, no Tz-based conjugated polymers have been reported for photocatalytic hydrogen evolution.

In this study, we investigate Tz as a new acceptor motif for D–A conjugated polymer photocatalysts. Inspired by the electron-withdrawing nature and hydrogen-binding capability of the BT unit, we designed and synthesized a novel Tz-based acceptor monomer, 2,5-bis(5-bromo-4-octylthiazol-2-yl)thiophene (OTzT). This molecule features two 4-octylthiazole (OTz) units connected to a central thiophene core, thereby positioning a nitrogen atom from the thiazole ring and a sulfur atom from the thiophene ring in proximity—mimicking the active binding configuration found in BT. For comparison, we also synthesized 5,5′-dibromo-4,4′-dioctyl-2,2′-bithiazole (OTz), a similar structure lacking the thiophene core.

These two acceptor monomers were copolymerized with a fluorene-based donor monomer, 2,2′-(9,9-dioctyl-9*H*-fluorene-2,7-diyl)bis(4,4,5,5-tetramethyl-1,3,2-dioxaborolane), yielding two D–A conjugated polymers: **PFOTzT** and **PFOTz**. The only structural difference between the two lies in the presence (**PFOTzT**) or absence (**PFOTz**) of a thiophene spacer between the two OTz rings. The thiophene spacer not only enhances intramolecular charge transfer (ICT) between the donor and acceptor units but also reduces the polymer's optical bandgap *via* LUMO stabilization and HOMO destabilization.[41] Furthermore, the increased π-conjugation length and extended spacing between OTz units in **PFOTzT** may provide improved accessibility and more favorable active sites for hydrogen evolution.[42] The discovery of alternative conjugated polymers beyond BT-based systems will serve as an important starting point for the advancement of metal-free photocatalysis.

Results and discussion

Synthesis and characterization

2-Bromo-4-octylthiazole and 2,5-bis(trimethylstannyl)thiophene were synthesized according to previously reported procedures. Compound **1** (Fig. S1) was prepared *via* a Stille coupling reaction between 2,5-bis(trimethylstannyl)thiophene and 2-bromo-4-octylthiazole in the presence of a palladium catalyst. Subsequent bromination of compound **1** with *N*-bromosuccinimide (NBS) in DMF afforded the final monomer, compound **2** (Fig. S2). Compound **3** (Fig. S3) was synthesized through a heterocyclic ring-forming reaction between 1-bromooctan-2-one and dithiooxamide. The final monomer, compound **4** (Fig. S4), was then obtained by brominating compound **3** with NBS in a DMF/acetic acid co-solvent system. The D–A conjugated polymers **PFOTzT** and **PFOTz** were synthesized *via* the Suzuki coupling polycondensation of the fluorene-based donor monomer with compounds **2** and **4**, respectively, in the presence of a palladium catalyst and a suitable base. To ensure full termination of the polymer chain ends and to eliminate any residual reactivity, 1-bromobenzene and 4,4,5,5-tetramethyl-2-phenyl-1,3,2-dioxaborolane were sequentially introduced for end-capping, yielding the final polymers **PFOTzT** and **PFOTz** with both ends capped (Scheme 1). The success of the end-capping procedure was confirmed by the disappearance of terminal boronic ester and bromoarene signals from the ^{1}H NMR spectra (Fig. S5–S8).[43] This end capping ensures that the observed differences in optical and photocatalytic properties arise solely from the polymer backbone design, rather than from chain-end effects.

The absorption spectra of the synthesized polymers and their nanoparticles were investigated (Fig. 1a and b). In the thin-film state (Fig. 1a), **PFOTzT** continues to exhibit stronger vibronic features and more pronounced 0–1 transitions than **PFOTz**, reflecting the enhanced backbone planarity and intramolecular ordering facilitated by the thiophene spacer. To investigate how different nanoparticle formation strategies affect molecular ordering and aggregation behavior, **PFOTzT** and **PFOTz** nanoparticles were prepared using two established techniques: mini-emulsion and nanoprecipitation.[44,45] The mini-emulsion approach utilizes ultrasonication with surfactants such as sodium dodecyl sulfate (SDS) or 2-(3-thienyl)ethyloxybutylsulfonate sodium salt (TEBS) to yield colloidally stable particles with well-controlled sizes. In contrast, the nanoprecipitation method induces polymer aggregation under aqueous conditions using amphiphilic stabilizers like PEG–COOH (PEG), resulting in distinct surface environments and morphologies. The absorption trend seen for thin films is further amplified upon nanoparticle formation, where **PFOTzT** demonstrates enhanced aggregation and molecular ordering (Fig. 1b and Fig. S9). These structural advantages contribute to improved exciton transport and charge separation, which are crucial in organic photocatalysts lacking high dielectric constants or internal junctions.[46,47] The ordered crystalline domains in **PFOTzT** nanoparticles facilitate exciton migration and dissociation, ultimately enabling more efficient charge carrier transport to reactive sites.[48,49]

Spectroscopic analyses revealed notable differences in optical absorption and aggregation states, and we further investigated how these structural variations influence the electronic properties of the polymers by conducting cyclic voltammetry tests. Cyclic voltammetry (CV) data (Fig. 1c) reveal key differences in the electronic structures of the polymers. **PFOTzT**, featuring

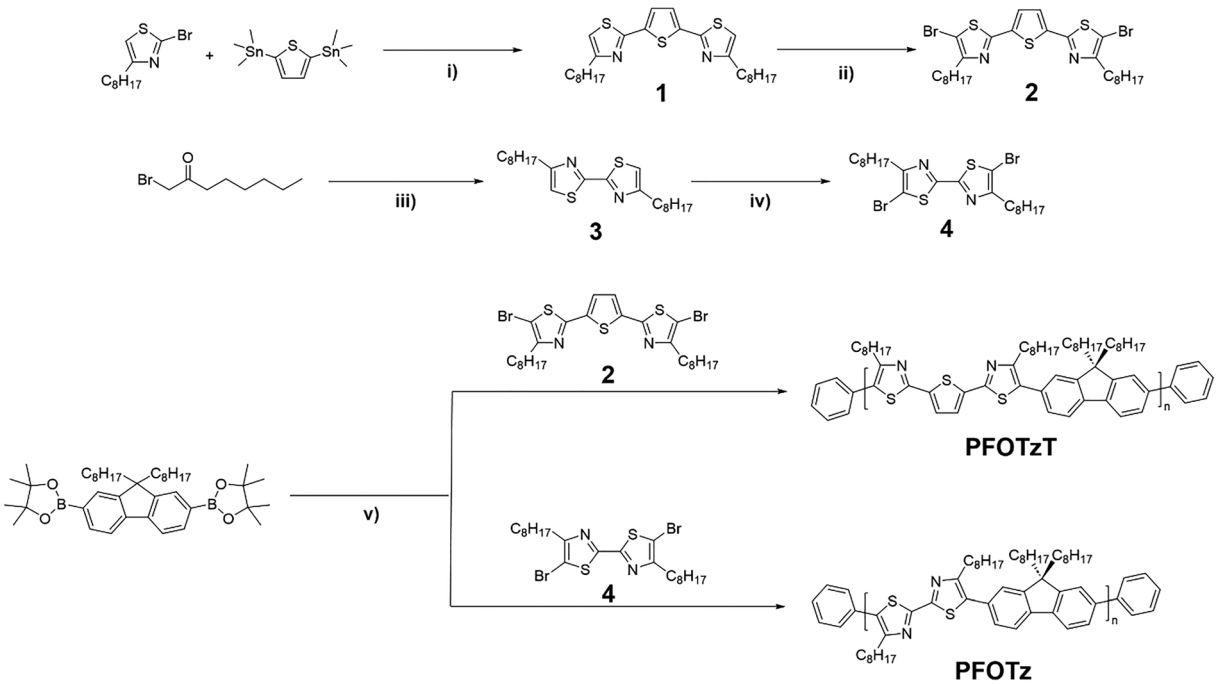

Scheme 1 Synthetic routes to OTz-based monomers and polymers (**PFOTzT** and **PFOTz**). Reaction conditions: (i) $Pd(PPh_3)_4$, toluene, 110 °C; (ii) NBS, DMF; (iii) dithiooxamide, dithiooxamide, ethanol; (iv) NBS, DMF/AcOH; (v) Aliquat 336, $Pd(PPh_3)_4$, 2 M K_3PO_4, toluene, 110 °C.

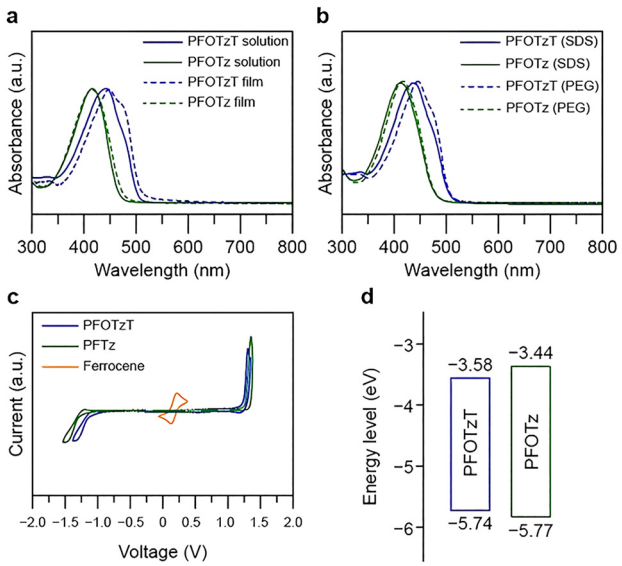

Fig. 1 UV-vis absorption spectra of the polymers (a) in solution and film states and (b) as nanoparticles prepared *via* mini-emulsion (SDS) and nanoprecipitation (PEG). (c) Cyclic voltammograms of the polymers and (d) HOMO/LUMO energy level diagrams of the polymers in the neutral state from CV and optical band gap measurements.

Table 1 A summary of the optical and electrochemical properties of the polymers

Polymer	λ_{max} (nm) Solution	λ_{max} (nm) Film	$\lambda_{onset,film}$ (nm)	E_g^{opt} (eV)	E_{HOMO} (eV)	E_{LUMO} (eV)
PFOTzT	441	477, 474	506	2.45	−5.74	−3.58
PFOTz	415	414	472	2.62	−5.77	−3.44

thiophene and OTz units, displays a stabilized LUMO energy level at −3.58 eV, compared to −3.44 eV for **PFOTz**. Both polymers share nearly identical HOMO levels (−5.74 eV for **PFOTzT** and −5.77 eV for **PFOTz**), due to their common donor backbone (Fig. 1d). The reduced bandgap of **PFOTzT** originates from its thiophene-extended Tz acceptor unit, which is expected to enable broader light absorption and more efficient charge separation. These electronic differences, reflected in the optical and electrochemical properties summarized in Table 1, correlate with the improved photocatalytic activity observed in subsequent experiments.

The molecular weights of **PFOTzT** and **PFOTz** were measured by gel permeation chromatography, and the number-average molecular weights of **PFOTzT** and **PFOTz** were 59 and 35 kDa, respectively (Fig. S6 and S8). This moderate difference in molecular weight is unlikely to affect the intrinsic electronic structure or photocatalytic performance, confirming that the observed differences in activity primarily stem from the backbone architecture rather than the chain length.

Photocatalytic hydrogen evolution performance

Building on the structural and optical differences observed in solution, thin film, and nanoparticle states, we next investigated how these variations affect the photocatalytic hydrogen evolution reaction (HER) efficiency. Given the critical role of interfacial environments in mediating exciton dissociation and charge transport, HER measurements were performed using

PFOTzT and **PFOTz** nanoparticles synthesized *via* both mini-emulsion and nanoprecipitation methods using different surfactants.

To establish a clear relationship between nanoparticle morphology and photocatalytic activity, both the mini-emulsion and nanoprecipitation approaches were adopted. The mini-emulsion route is known to produce kinetically trapped dispersions under ultrasonication, in which surfactant molecules reside at the polymer–water interface and help regulate surface charge and hydration. In our case, this method gave relatively uniform particles with controlled size and good colloidal stability, allowing a systematic comparison of how interfacial structure correlates with charge transport and reactivity. In contrast, nanoprecipitation relies on rapid diffusion between a good solvent and water, with polymer chains spontaneously aggregating as the solvent is displaced. This approach often proceeds without added surfactants because transient solvent stabilization can provide short-term colloidal stability; however, highly π-conjugated polymers, such as our Tz–thiophene system, can undergo pronounced aggregation during fast solvent exchange. To mitigate uncontrolled coalescence and maintain reasonable molecular ordering, we added a small amount of PEG as a soft stabilizer. Its non-ionic and hydrophilic ether backbone is expected to provide gentle interfacial stabilization while only weakly perturbing the intrinsic π–π interactions of the conjugated polymer. Rather than forming well-defined micelles, PEG is likely to adsorb weakly onto the polymer backbone, slowing down solvent–antisolvent interdiffusion and favouring more uniform particle nucleation. Under these conditions, we were able to reproducibly prepare stable dispersions suitable for comparing photocatalytic performance across different processing routes.[49]

HER measurements were performed under AM 1.5G illumination using 1.0 M ascorbic acid (AA) (pH 4.0) as a sacrificial donor. The incident light intensity was maintained at 100 mW cm^{-2}, and the reactions were conducted in glass vials with a diameter of 3 cm under ambient temperature and pressure conditions in the laboratory. Across all methods, **PFOTzT** nanoparticles consistently outperformed **PFOTz** (Fig. 2 and Table 2). Notably,

Table 2 A summary of HER measurements

HER (μmol g^{-1} h^{-1})	TEBS	PEG	SDS
PFOTzT	246.8	181.9	102.4
PFOTz	35.0	10.0	13.9

PFOTzT/TEBS nanoparticles achieved the highest HER activity of 246.8 μmol g^{-1} h^{-1}, exceeding the performance of **PFOTz**/TEBS (35 μmol g^{-1} h^{-1}) over seven-fold. ICP-MS confirmed negligible residual Pd content, validating the intrinsic photocatalytic activity of the polymers.[50]

The superior performance of **PFOTzT** is attributed to its enhanced molecular crystallinity and broader absorption profile. Across all nanoparticle formulations, **PFOTzT** consistently exhibited higher hydrogen evolution activity than **PFOTz**, reflecting the intrinsic advantages arising from its backbone design. The insertion of a thiophene spacer between Tz units extends π-conjugation and increases backbone planarity. This structural modification promotes efficient intramolecular charge delocalization and optimized orbital overlap, leading to superior exciton transport despite the moderate long-range crystallinity. Two-dimensional grazing incidence X-ray diffraction (2D-GIXD) analysis was conducted to understand the difference in the molecular ordering. As shown in Fig. S15, although the polymer nanoparticles are randomly oriented isotropic spheres (resulting in ring-like diffraction patterns rather than distinct spots), clear diffraction peaks from lamellar and π–π stacking are still observed for **PFOTzT**. This indicates that molecular ordering and crystalline domains are preserved even within the confined nanostructures, driven by the self-assembling tendency of the **PFOTzT** backbone. In contrast, **PFOTz** exhibited broad halo patterns, indicating a predominantly amorphous nature. Therefore, the enhanced crystallinity and long-range packing of **PFOTzT** also contribute to its superior performance. Moreover, the stabilized LUMO level of **PFOTzT** also facilitates electron transfer to protons, while its red-shifted absorption enables broader light harvesting under solar illumination. These combined optical, electrochemical, and structural benefits provide a fundamentally more favorable framework for charge separation

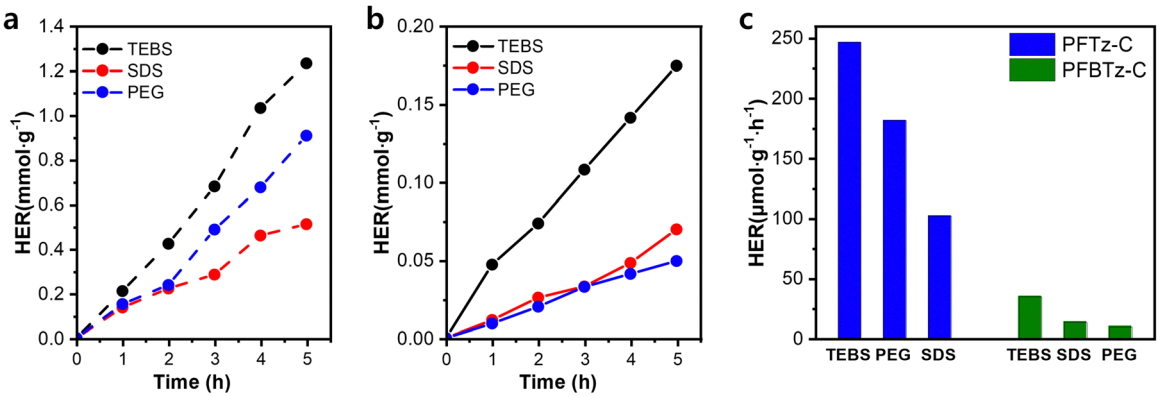

Fig. 2 (a) and (b) Time-dependent photocatalytic hydrogen evolution activities of **PFOTzT** and **PFOTz** nanoparticles obtained using TEBS, PEG, and SDS surfactants. (c) A comparison of the photocatalytic HER activity by surfactant type under AM 1.5G illumination with 1.0 M ascorbic acid (pH 4.0).

and photocatalytic redox processes, explaining the markedly higher HER activity observed for **PFOTzT** nanoparticles.

Among the tested surfactants, TEBS yielded the highest hydrogen evolution rate, while PEG showed moderate activity, and SDS produced the lowest. Although TEBS-stabilized nanoparticles exhibit a slightly larger hydrodynamic diameter compared to SDS-stabilized ones (Fig. 3), this is attributed to the formation of a more open and highly hydrated surfactant shell at the particle–water interface. Unlike a compact solid surface, such a swollen interfacial layer enhances water penetration and provides local dielectric screening. These factors significantly improve the exciton dissociation efficiency and facilitate interfacial charge-transfer processes, effectively compensating for any potential loss in activity due to the modest decrease in the geometric surface-to-volume ratio,[51,52] providing favorable conditions for exciton dissociation and redox reactions. In contrast, PEG generated moderately hydrophilic but electronically inert interfaces, and SDS formed compact shells that restricted water access and charge transport. To clarify the molecular origins of these differences, the interfacial characteristics of each surfactant were further analyzed.

Under identical mini-emulsion conditions, SDS and TEBS both produced stable dispersions, yet the resulting interfacial environments were fundamentally different. SDS, consisting of a long alkyl chain and a sulfate headgroup, forms a compact ionic shell that limits water penetration and suppresses interfacial electron transfer. In contrast, TEBS contains a thiophene–sulfonate motif capable of π–π and S···S interactions with the conjugated backbone. These interactions improve molecular alignment and create a hydrated polar interface that facilitates exciton separation. Although TEBS does not form micelles or bind strongly to particle surfaces, its thiophene unit can penetrate the near-surface amorphous domains of the polymer, creating localized π–π contacts and partial electronic coupling. Its flexible aromatic structure allows weak but electronically active contacts that effectively mediate exciton dissociation and electron transfer; this is consistent with the higher HER activity observed for TEBS-based nanoparticles compared to SDS-based ones.

The comparison between TEBS and PEG further highlights the structural origin of interfacial effects.[53,54] While both surfactants exhibit strong hydrophilicity, PEG consists of non-conjugated ether chains that form a thick amorphous hydration layer but cannot engage in π–π interactions with the polymer backbone. During nanoprecipitation, this hydrated layer acts as a dielectric barrier that reduces internal ordering and slows charge transport. Conversely, TEBS features a π-conjugated thiophene ring that maintains local alignment with the bithiazole–thiophene backbone, even during the dynamic mini-emulsion process. Its sulfonate headgroup also increases interfacial polarity and promotes water diffusion, collectively leading to more efficient exciton dissociation and electron transfer. These combined properties render TEBS an effective compatibilizer, bridging hydrophilic solvation and π-electronic coupling, which explains its superior HER performance compared to PEG-stabilized nanoparticles.

The AQYs of the **PFOTzT**/TEBS nanoparticles were measured by using monochromatic light filters to verify the photo-driven nature of the reaction. As shown in Fig. S16, the AQY values closely follow the trend of the polymer's UV-vis absorption profile. This finding confirms that the hydrogen evolution reaction is intrinsically driven by light absorption by the **PFOTzT** backbone, rather than by impurities or other artifacts.

The HER performances of linear conjugated polymers are summarized in Table S1. Most reported systems are based on BT-containing polymers, and high HER activity without the use of a Pt co-catalyst remains extremely rare.[28,48,50,55–57] Notably, the **PFOTzT**/TEBS nanoparticles show a promising HER activity of 0.25 mmol g^{-1} h^{-1} without the use of any co-catalyst. These results demonstrate that our rational backbone engineering strategy, combined with surfactant-assisted processing, effectively overcomes the intrinsic limitations of linear polymers, thereby establishing Tz-based polymers as highly promising candidates for use in next-generation photocatalysts.

Exciton dynamics and charge separation

To assess the efficiency of exciton separation and charge generation in different nanoparticle systems, we first performed steady-state photoluminescence (SS-PL) measurements (Fig. 4). PL spectra were recorded under identical optical conditions, and the optical densities of all samples were carefully adjusted to achieve equal absorbance ($A \approx 0.4$) at the excitation wavelength. This normalization ensured that the

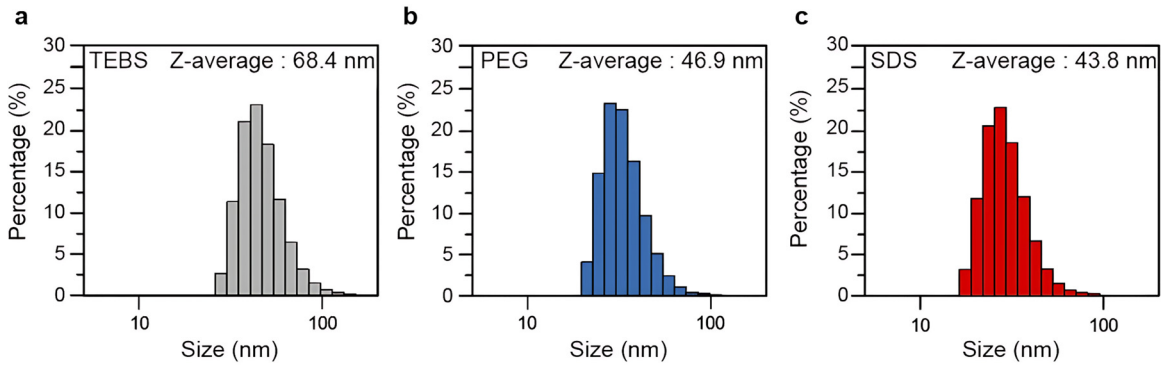

Fig. 3 Size distributions of nanoparticles prepared with (a) TEBS, (b) PEG, and (c) SDS surfactants in aqueous media.

observed changes in PL intensity reflect intrinsic photophysical variations rather than differences in the absorbed excitation power. SS-PL analysis revealed a strong correlation between the exciton quenching yield and HER activity, further confirming the role of interfacial modification by surfactants (Fig. S10). PL spectroscopy revealed that **PFOTzT**/TEBS exhibited a quenching yield of 94.05%, indicating highly efficient exciton separation. PEG and SDS systems showed lower yields, with SDS displaying an anomalous PL increase upon AA addition, suggesting poor charge separation. This observation suggests diminished charge-transfer efficiency and higher levels of insulating behavior in SDS-stabilized systems. **PFOTz** followed a similar surfactant-dependent trend, with TEBS yielding the highest quenching (99.37%), although its absolute HER activity remained lower, likely due to its less-ordered internal structure and reduced long-range charge transport (Fig. S11). Interestingly, **PFOTzT** exhibited consistently lower PL intensities than **PFOTz**, reflecting more efficient non-radiative decay *via* charge separation pathways rather than radiative recombination.[58]

The SS-PL spectra revealed distinct behaviors of **PFOTzT**-based nanoparticles depending on the type of surfactant employed. In the studied systems, AA generally induced a decrease in emission intensity due to its role as an electron donor; however, partial PL enhancement was observed only for the **PFOTzT**/SDS sample, whereas the PEG- and TEBS-stabilized systems exhibited conventional quenching. The selective PL increase in the **PFOTzT**/SDS system suggests that AA induces subtle structural rearrangements in the polymer domains when a rigid, insulating surfactant shell is present.[59] SDS forms a dense ionic interface that initially restricts water penetration and limits exciton diffusion. Upon the introduction of AA, the interfacial environment becomes more polar, weakening the tight packing of SDS molecules and allowing partial reorganization of the polymer surface. This relaxation can promote the formation of locally ordered emissive regions, thereby increasing the probability of radiative recombination in **PFOTzT**/SDS nanoparticles. In contrast, the TEBS- and PEG-stabilized systems already possess hydrated, flexible interfaces, where AA mainly facilitates charge extraction rather than structural rearrangement, resulting in continued PL quenching.[60,61]

Importantly, the **PFOTz**/SDS system does not show any PL enhancement under identical conditions. This behavior is likely related to the less-flexible backbone of **PFOTz**, which likely limits the interchain reorganization and optimization of π–π interactions at the SDS-modified interface. Without such structural relaxation, the radiative pathways appear to remain largely unchanged, and AA primarily acts as a reductive quencher, resulting in the observed monotonic PL decrease.

These results together indicate that the mild PL enhancement observed only in **PFOTzT**/SDS originates from the morphology-driven redistribution of emissive domains enabled by the thiophene-spaced, more-flexible backbone, whereas other surfactant systems remain dominated by charge-transfer-induced quenching behavior.

Time-resolved PL (TR-PL) measurements were then conducted to further probe exciton lifetimes and potential recombination pathways (Fig. S12). The results indicated that exciton radiative decay occurs within a few nanoseconds for both **PFOTzT** and **PFOTz**, confirming the rapid exciton recombination kinetics. TR-PL analysis showed that **PFOTzT** nanoparticles had longer exciton lifetimes than **PFOTz** in the absence of AA, consistent with their crystalline structure and low recombination rates (Fig. S13). Upon AA addition, lifetimes shortened significantly, indicating efficient charge separation. To directly examine the charge carrier dynamics, we employed nano-microsecond transient absorption spectroscopy (TAS), enabling us to track the evolution of photoinduced species over time. The TA spectra, observed in the range of 400 nm to 800 nm, provided insights into interfacial modification induced by different surfactants (Fig. 5). The ground-state bleaching (GSB) signal at 450 nm corresponded to the UV-vis absorbance region, indicating that **PFOTzT** exhibits efficient long-lived charge carrier generation upon light exposure, irrespective of the surfactant used. Additionally, the photoinduced absorption (PIA) signal at 600 nm showed a positive differential optical density (ΔOD) in the absence of AA but exhibited quenching when AA was introduced. Most notably, TEBS-stabilized **PFOTzT** nanoparticles show ultrafast quenching of both the GSB and PIA signals within the instrument response time (<10 ns), corresponding to a quenching efficiency exceeding 99%, which clearly indicates a barrier-free interface enabling highly efficient electron transfer with AA. In contrast, **PFOTzT**/SDS exhibits negligible quenching (<5%), with decay dynamics in the presence of AA ($\tau_{1/2} \approx 900$ ns) nearly identical to those in the pristine state, confirming that the

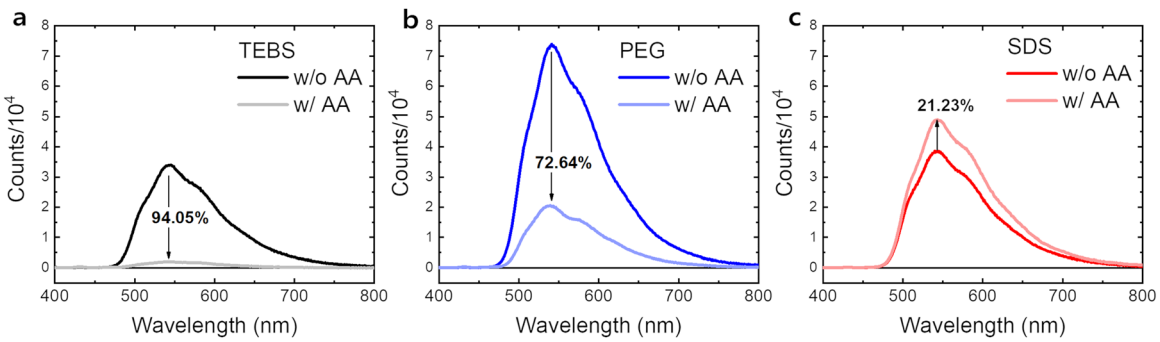

Fig. 4 Steady-state PL spectra of **PFOTzT** nanoparticles stabilized with (a) TEBS, (b) PEG, and (c) SDS, measured before and after ascorbic acid addition.

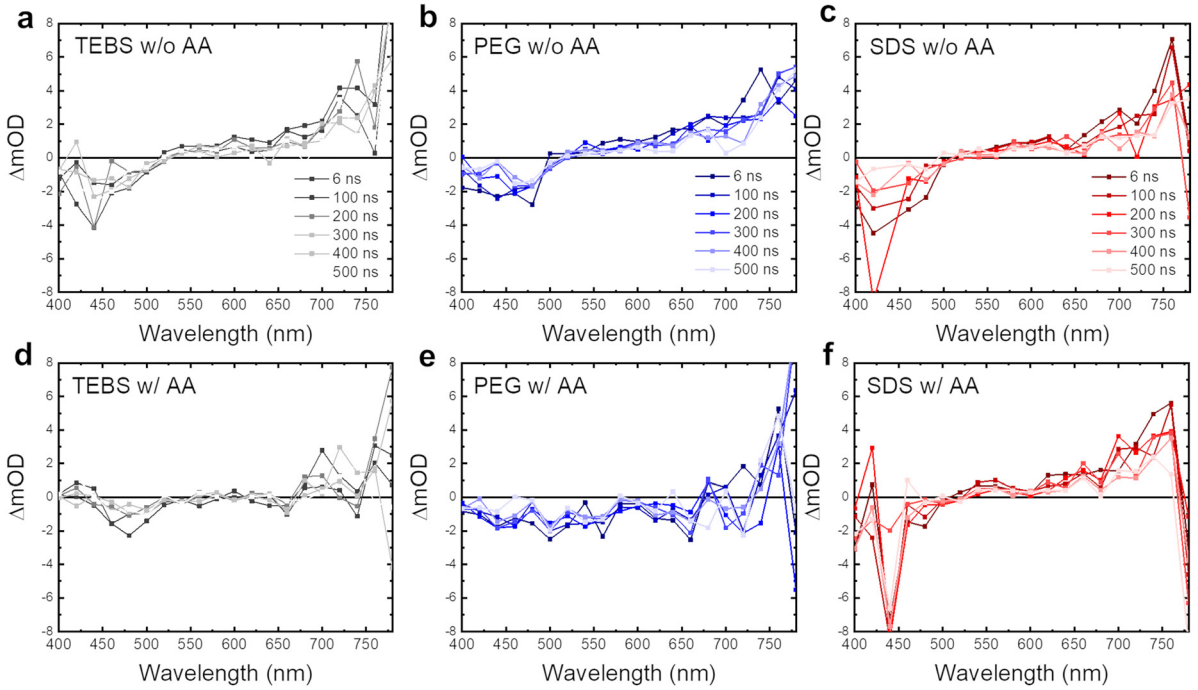

Fig. 5 Transient absorption spectra of **PFOTzT** nanoparticles stabilized with (a) and (d) TEBS, (b) and (e) PEG, and (c) and (f) SDS, measured without AA (a)–(c) and with AA (d)–(f). Spectra were recorded after various delay times (6–500 ns) following 355-nm pulsed excitation.

insulating SDS shell suppresses interfacial charge extraction and leads to charge accumulation. **PFOTzT**/PEG shows negative transient signals upon AA addition, indicative of charge trapping behaviour, consistent with its moderate photocatalytic performance (Table S1). Moreover, the TA spectra also revealed that TEBS-stabilized **PFOTz** generated few charge carriers in the visible-light region, aligning with the observed HER performance (Fig. S14).[62,63]

As shown in Fig. 6a, the kinetic profiles of the ground-state bleaching (GSB) signals revealed comparable charge carrier lifetimes across different surfactant systems, consistent with the corresponding transient absorption (TA) spectra. To gain further insights into the electron dynamics, the kinetics at 600 nm were analyzed (Fig. 6b–d). **PFOTzT** nanoparticles stabilized with PEG exhibited persistent GSB signals within the range of 400–500 nm and retained a positive ΔOD in the absence of AA, which reversed to a negative ΔOD upon AA addition, suggesting the presence of trapped or accumulated charges. In contrast, SDS-stabilized nanoparticles showed minimal spectral changes in the presence of AA, indicating inefficient interfacial charge transfer. For TEBS-stabilized **PFOTzT**, a pronounced positive ΔOD, attributed to long-lived charge carriers, was observed without AA, whereas this signal was almost completely quenched with AA, indicative of rapid and efficient interfacial charge transfer and consistent with the superior hydrogen evolution activity of the TEBS-based system.

These observations were further corroborated by the analysis of both GSB and photoinduced absorption (PIA) signals (Fig. 6), which collectively demonstrated that TEBS yields the highest population of long-lived charge carriers capable of

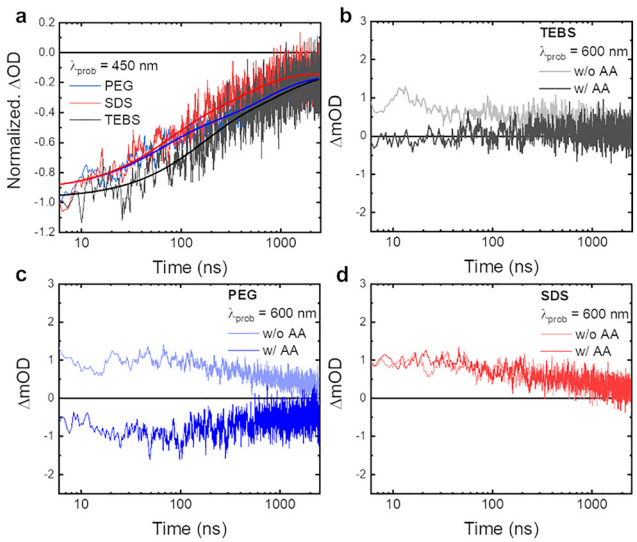

Fig. 6 (a) GSB decay at 450 nm for **PFOTzT** nanoparticles, revealing the exciton lifetime dynamics in the absence of AA. (b)–(d) PIA decay at 600 nm for **PFOTzT** nanoparticles stabilized with TEBS, PEG, and SDS, respectively, measured with and without AA.

interfacial transfer. This enhancement is likely facilitated by the increased local permittivity and reduced exciton diffusion lengths associated with the TEBS interface. Although the **PFOTzT**/SDS system exhibits the strongest initial GSB signal intensity, this should not be interpreted as the system having high catalytic potential. Instead, this indicates the accumulation of photogenerated charges that are unable to participate in

surface redox reactions. Due to the dense and insulating nature of the SDS shell, interfacial electron transfer involving AA is severely impeded. Consequently, these trapped carriers do not undergo efficient quenching, leading to both a persistent GSB signal and the poorest hydrogen evolution performance.

Conclusions

This study demonstrates that the precise backbone engineering of Tz-based conjugated polymers can significantly influence the photocatalytic hydrogen evolution performance. Through a direct comparison of **PFOTzT** and **PFOTz**, we show that inserting a thiophene spacer between Tz units leads to enhanced π-conjugation, extended electron delocalization, improved interfacial wettability with the aqueous medium, and broader light absorption. Among the various nanoparticle formulations, **PFOTzT** nanoparticles stabilized by TEBS exhibited the highest hydrogen evolution rate (246.8 μmol g^{-1} h^{-1}), outperforming **PFOTz** over seven-fold under identical conditions. This performance is attributed to synergistic effects between the polymer's intermolecular ordering and the surfactant-induced interfacial environment, which jointly facilitate water penetration, suppress recombination, and promote exciton dissociation. These findings underscore that achieving high-efficiency photocatalysis requires not only the rational design of semiconducting polymers but also the precise engineering of nanoparticle interfaces to optimize charge transport pathways and minimize recombination losses.

Author contributions

Taekmin Kim: data curation: equal; formal analysis: equal; investigation: equal; methodology: equal; writing – original draft: equal; WonJo Jeong: data curation: equal; formal analysis: equal; investigation: equal; methodology: equal; writing – original draft: equal; Sanghyeok An: data curation: supporting; formal analysis: supporting; investigation: supporting; methodology: supporting; writing – original draft: supporting; Junho Kim: data curation: supporting; formal analysis: supporting; investigation: supporting; methodology: supporting; Gayoung Ham: formal analysis: supporting; investigation: supporting; visualization: supporting; Seungok Pyo: data curation: supporting; visualization: supporting; Hyojung Cha: resources: equal; supervision: equal; validation: equal; writing – review & editing: equal; In Hwan Jung: conceptualization: equal; funding acquisition: equal; project administration: equal; resources: equal; supervision: equal; writing – review & editing: equal; Dae Sung Chung: conceptualization: equal; funding acquisition: equal; project administration: equal; resources: equal; supervision: equal; writing – review & editing: equal.

Conflicts of interest

There are no conflicts to declare.

Data availability

The authors declare that all data supporting the findings of this study are available within the article and its supplementary information (SI). The SI contains detailed experimental procedures, characterization data (NMR, GPC), spectroscopic analyses (PL, TRPL, TAS), structural characterization (2D-GIXD), and summary tables for photocatalytic performance. See DOI: https://doi.org/10.1039/d5nh00704f.

Any other data that support the findings of this study are available from the corresponding author upon reasonable request.

Acknowledgements

Taekmin Kim and WonJo Jeong contributed equally to this work. This study was supported by the National Research Foundation of Korea (RS-2022-NR068160) and Ministry of Trade, Industry and Energy (RS-2024-00422305).

References

1 D. J. Martin, P. J. T. Reardon, S. J. A. Moniz and J. Tang, *J. Am. Chem. Soc.*, 2014, **136**, 12568–12571.
2 H. Nishiyama, T. Yamada, M. Nakabayashi, Y. Maehara, M. Yamaguchi, Y. Kuromiya, Y. Nagatsuma, H. Tokudome, S. Akiyama, T. Watanabe, R. Narushima, S. Okunaka, N. Shibata, T. Takata, T. Hisatomi and K. Domen, *Nature*, 2021, **598**, 304–307.
3 K. Maeda and K. Domen, *J. Phys. Chem. Lett.*, 2010, **1**, 2655–2661.
4 Y. Liu, Q. Gao, L. Shi, J. Kearney, X. Han, Z. Xie, M. Wang, H. Zhou and H. Zhu, *Nanoscale Horiz.*, 2025, **10**, 2037–2044.
5 D. Datta, R. Mondal, R. C. Maji, S. Yu, D.-I. Won, D. H. Kim and S. K. Maji, *Nanoscale Horiz.*, 2025, **10**, 3453–3468.
6 D. L. Ashford, M. K. Gish, A. K. Vannucci, M. K. Brennaman, J. L. Templeton, J. M. Papanikolas and T. J. Meyer, *Chem. Rev.*, 2015, **115**, 13006–13049.
7 I. Tsuji, H. Kato, H. Kobayashi and A. Kudo, *J. Am. Chem. Soc.*, 2004, **126**, 13406–13413.
8 J. Huang, K. L. Mulfort, P. Du and L. X. Chen, *J. Am. Chem. Soc.*, 2012, **134**, 16472–16475.
9 Z. Han, F. Qiu, R. Eisenberg, P. L. Holland and T. D. Krauss, *Science*, 2012, **338**, 1321–1324.
10 Y.-S. Chen and P. V. Kamat, *J. Am. Chem. Soc.*, 2014, **136**, 6075–6082.
11 H. Zheng, B. Zi, T. Zhou, G. Qiu, Z. Luo, Q. Lu, A. R. P. Santiago, Y. Zhang, J. Zhao, J. Zhang, T. He and Q. Liu, *Nanoscale Horiz.*, 2024, **9**, 1532–1542.
12 F. Sun, K. Yang, X. Qin, W. Wu and Y. Lu, *Nanoscale Horiz.*, 2025, **10**, 1120–1130.
13 M. V. Pavliuk, S. Wrede, A. Liu, A. Brnovic, S. Wang, M. Axelsson and H. Tian, *Chem. Soc. Rev.*, 2022, **51**, 6909–6935.
14 G. Kumar, B. Cai, S. Ott and H. Tian, *Chem. Phys. Rev.*, 2023, **4**, 011307.

15 A. M. Elewa, C.-Y. Liao, W.-L. Li, I. M. A. Mekhemer and H.-H. Chou, *Macromolecules*, 2023, **56**, 1352–1361.
16 J. Byun and K. A. I. Zhang, *Mater. Horiz.*, 2020, **7**, 15–31.
17 C.-L. Chang, W.-C. Lin, L.-Y. Ting, C.-H. Shih, S.-Y. Chen, T.-F. Huang, H. Tateno, J. Jayakumar, W.-Y. Jao, C.-W. Tai, C.-Y. Chu, C.-W. Chen, C.-H. Yu, Y.-J. Lu, C.-C. Hu, A. M. Elewa, T. Mochizuki and H.-H. Chou, *Nat. Commun.*, 2022, **13**, 5460.
18 T. Banerjee, F. Podjaski, J. Kröger, B. P. Biswal and B. V. Lotsch, *Nat. Rev. Mater.*, 2021, **6**, 168–190.
19 J. Spears, M. Shawky Adly, E. Castro, A. R. Puente Santiago, L. Echegoyen, T. He, C. J. Dares and M. Noufal, *Nanoscale Horiz.*, 2025, **10**, 719–723.
20 A. Chen, X. Li, J. Wang and J. Zhang, *Energy Mater. Adv.*, 2023, **4**, 0028.
21 X. Hu, X. Yang, B. Song, Z. Zhan, R. Sun, Y. Guo, L.-M. Yang, X. Yang, C. Zhang, I. Hussain, X. Wang and B. Tan, *SusMat*, 2024, **4**, e220.
22 A. F. Saber, A. M. Elewa, H.-H. Chou and A. F. M. El-Mahdy, *ChemCatChem*, 2023, **15**, e202201287.
23 I. Jalan, C. F. N. Marchiori, Z. Genene, A. Johansson, C. M. Araujo, E. Wang, J. van Stam and E. Moons, *J. Mater. Chem. C*, 2023, **11**, 9316–9326.
24 Y. I. A. Reyes, L.-Y. Ting, X. Tu, H.-Y. T. Chen, H.-H. Chou and C. Coluccini, *Appl. Sci.*, 2020, **10**, 7017.
25 J. Kosco and I. McCulloch, *ACS Energy Lett.*, 2018, **3**, 2846–2850.
26 C. M. Aitchison and I. McCulloch, *Chem. Mater.*, 2024, **36**, 1781–1792.
27 R. J. Lyons and R. S. Sprick, *Mater. Horiz.*, 2024, **11**, 3764–3791.
28 P. B. Pati, G. Damas, L. Tian, D. L. A. Fernandes, L. Zhang, I. B. Pehlivan, T. Edvinsson, C. M. Araujo and H. Tian, *Energy Environ. Sci.*, 2017, **10**, 1372–1376.
29 S. An, K.-J. Jeong, S. Z. Hassan, G. Ham, S. Kang, J. Lee, H. Ma, J. Kwon, S. Y. Jeong, J. Yang, H. Y. Woo, H.-H. Cho, H. Cha, C. Y. Son and D. S. Chung, *Adv. Sci.*, 2024, **11**, 2309786.
30 M. Axelsson, Z. Xia, S. Wang, M. Cheng and H. Tian, *JACS Au*, 2024, **4**, 570–577.
31 M. Axelsson, C. F. N. Marchiori, P. Huang, C. M. Araujo and H. Tian, *J. Am. Chem. Soc.*, 2021, **143**, 21229–21233.
32 A. Liu, C.-W. Tai, K. Holá and H. Tian, *J. Mater. Chem. A*, 2019, **7**, 4797–4803.
33 Y. Bai, K. Hippalgaonkar and R. S. Sprick, *J. Mater. Chem. A*, 2021, **9**, 16222–16232.
34 D. Tuncel and H. V. Demir, *Nanoscale*, 2010, **2**, 484–494.
35 S. Kang, T. W. Yoon, G.-Y. Kim and B. Kang, *ACS Appl. Nano Mater.*, 2022, **5**, 17436–17460.
36 J. Kosco, M. Bidwell, H. Cha, T. Martin, C. T. Howells, M. Sachs, D. H. Anjum, S. Gonzalez Lopez, L. Zou, A. Wadsworth, W. Zhang, L. Zhang, J. Tellam, R. Sougrat, F. Laquai, D. M. DeLongchamp, J. R. Durrant and I. McCulloch, *Nat. Mater.*, 2020, **19**, 559–565.
37 W. Zhang, X. Luo, H. Tang, Z. Tang, F. Huang, Q. Wan, G. Yu and H. Yang, *J. Mater. Chem. A*, 2025, **13**, 4746–4793.
38 H.-L. Su, D. N. Sredojevic, H. Bronstein, T. J. Marks, B. C. Schroeder and M. Al-Hashimi, *Macromol. Rapid Commun.*, 2017, **38**, 1600610.
39 Y. Teshima, K. Yamanaka, Y. Sato, H. Ohkita, T. Mikie, M. Saito and I. Osaka, *ACS Appl. Mater. Interfaces*, 2024, **16**, 3735–3743.
40 Y. Ie, M. Nitani, M. Karakawa, H. Tada and Y. Aso, *Adv. Funct. Mater.*, 2010, **20**, 907–913.
41 A. Liu, L. Gedda, M. Axelsson, M. Pavliuk, K. Edwards, L. Hammarström and H. Tian, *J. Am. Chem. Soc.*, 2021, **143**, 2875–2885.
42 L. Wang, R. Fernández-Terán, L. Zhang, D. L. A. Fernandes, L. Tian, H. Chen and H. Tian, *Angew. Chem., Int. Ed.*, 2016, **55**, 12306–12310.
43 U. Koldemir, S. R. Puniredd, M. Wagner, S. Tongay, T. D. McCarley, G. D. Kamenov, K. Müllen, W. Pisula and J. R. Reynolds, *Macromolecules*, 2015, **48**, 6369–6377.
44 A. Holmes, E. Deniau, C. Lartigau-Dagron, A. Bousquet, S. Chambon and N. P. Holmes, *ACS Nano*, 2021, **15**, 3927–3959.
45 M. Rammal, P. Lévêque, G. Schlatter, N. Leclerc and A. Hébraud, *Mater. Chem. Front.*, 2020, **4**, 2904–2931.
46 R. Yanagi, T. Zhao, D. Solanki, Z. Pan and S. Hu, *ACS Energy Lett.*, 2022, **7**, 432–452.
47 C. Xia, L. Yuan, H. Song, C. Zhang, Z. Li, Y. Zou, J. Li, T. Bao, C. Yu and C. Liu, *Small*, 2023, **19**, 2300292.
48 J. Kosco, S. Gonzalez-Carrero, C. T. Howells, T. Fei, Y. Dong, R. Sougrat, G. T. Harrison, Y. Firdaus, R. Sheelamanthula, B. Purushothaman, F. Moruzzi, W. Xu, L. Zhao, A. Basu, S. De Wolf, T. D. Anthopoulos, J. R. Durrant and I. McCulloch, *Nat. Energy*, 2022, **7**, 340–351.
49 A. Dolan, J. M. de la Perrelle, T. D. Small, E. R. Milsom, G. F. Metha, X. Pan, M. R. Andersson, D. M. Huang and T. W. Kee, *ACS Appl. Nano Mater.*, 2022, **5**, 12154–12164.
50 M. Sachs, H. Cha, J. Kosco, C. M. Aitchison, L. Francàs, S. Corby, C.-L. Chiang, A. A. Wilson, R. Godin, A. Fahey-Williams, A. I. Cooper, R. S. Sprick, I. McCulloch and J. R. Durrant, *J. Am. Chem. Soc.*, 2020, **142**, 14574–14587.
51 S. An, Z. Wu, H. Jeong, J. Lee, S. Y. Jeong, W. Lee, S. Kim, J. W. Han, J. Lim, H. Cha, H. Y. Woo and D. S. Chung, *Small*, 2023, **19**, 2204905.
52 S. Subianto, R. Balu, L. de Campo, A. Sokolova, N. K. Dutta and N. R. Choudhury, *ACS Appl. Mater. Interfaces*, 2018, **10**, 44116–44125.
53 K. N. Schwarz, S. B. Farley, T. A. Smith and K. P. Ghiggino, *Nanoscale*, 2015, **7**, 19899–19904.
54 A. Holmes, H. Laval, M. Guizzardi, V. Maruzzo, G. Folpini, N. Barbero, E. Deniau, M. Schmutz, S. Blanc, A. Petrozza, G. M. Paternò, G. Wantz, S. Chambon, C. Lartigau-Dagron and A. Bousquet, *Energy Environ. Sci.*, 2024, **17**, 1107–1116.
55 R. S. Sprick, L. Wilbraham, Y. Bai, P. Guiglion, A. Monti, R. Clowes, A. I. Cooper and M. A. Zwijnenburg, *Chem. Mater.*, 2018, **30**, 5733–5742.
56 A. Liu, S. Wang, H. Song, Y. Liu, L. Gedda, K. Edwards, L. Hammarström and H. Tian, *Phys. Chem. Chem. Phys.*, 2023, **25**, 2935–2945.
57 L. Tian, S. Guo, L. Feng, J. Wang, A. Wang and C.-X. Cui, *J. Mater. Chem. A*, 2024, **12**, 32164–32171.
58 D. M. E. Freeman, A. J. Musser, J. M. Frost, H. L. Stern, A. K. Forster, K. J. Fallon, A. G. Rapidis, F. Cacialli,

I. McCulloch, T. M. Clarke, R. H. Friend and H. Bronstein, *J. Am. Chem. Soc.*, 2017, **139**, 11073–11080.

59 A. Holmes, J. Pan, L. Wang, L. Franco, R. R. Bicudo, B. Albinsson, C. M. Araujo, W. Zhu, D. Wang, T.-Q. Nguyen, J. Zhu and E. Wang, *Adv. Mater.*, 2025, **37**, 2507702.

60 C. L. Donley, J. Zaumseil, J. W. Andreasen, M. M. Nielsen, H. Sirringhaus, R. H. Friend and J.-S. Kim, *J. Am. Chem. Soc.*, 2005, **127**, 12890–12899.

61 H. Piwoński, T. Michinobu and S. Habuchi, *Nat. Commun.*, 2017, **8**, 15256.

62 J. Zhang, B. Zhu, L. Zhang and J. Yu, *Chem. Commun.*, 2023, **59**, 688–699.

63 M. H. Elsayed, M. Abdellah, Y.-H. Hung, J. Jayakumar, L.-Y. Ting, A. M. Elewa, C.-L. Chang, W.-C. Lin, K.-L. Wang, M. Abdel-Hafiez, H.-W. Hung, M. Horie and H.-H. Chou, *ACS Appl. Mater. Interfaces*, 2021, **13**, 56554–56565.